博士論文（要約）

論文題目　　　Study on Plasma Induced Surface Modification of

Graphene Lattice

（プラズマによるグラフェン格子表面修飾の研究）

氏　　　名　　　赤田　圭史

Abstract

Graphene, an atomic layer of graphite packed in sp^2 hexagonal lattice, has attracted great attention for its superior properties. To expand potential use of graphene for various applications, surface modification is the promising methods to tailor the properties of graphene. Especially, work function of graphene tuned through doping or surface engineering can improve many electronics device technologies including organic semiconductor and field emission devices. However, the origin of work function tuning by surface modification has not been well understood.

Here, I doped nitrogen atoms to highly oriented pyrolytic graphite (HOPG) using N_2 plasma. The plasma treatment can provide a rich chemical environment, and enables surface modification of graphene without high temperature and toxic gases. Nitrogen doping site depends on surface defect of graphene: doping to inside of the graphene was dominant on defect-free HOPG, and doping to edge of the graphene was dominant on defective HOPG. From these results, I proved that the work function of graphene correlates strongly with the site and amount of doped nitrogen, and then I changed the work function in the range of 4.3 eV to 5.4 eV by selective nitrogen doping.

第４，５，６章は雑誌等で刊行予定のため非公開
５年以内に出版予定

Plasma assisted surface modification in this paper provides a valuable work function tuning of graphene and would open a way to tailor the nature of graphene for various industrial applications.
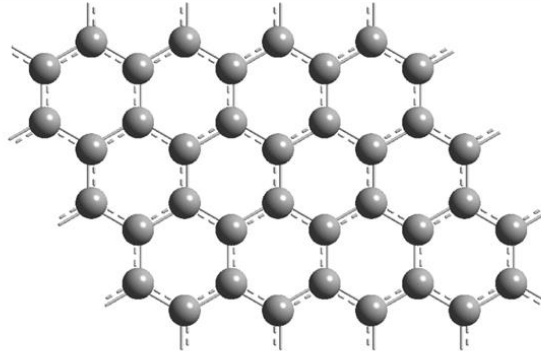
Contents

Chapter 1
Introduction
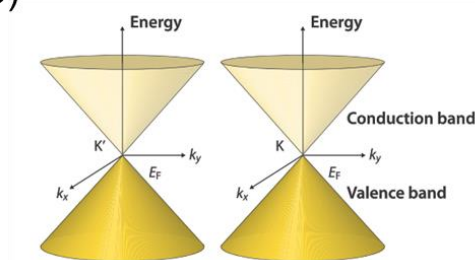
1.1 Background

1.1.1 Graphene

Graphene, a single layer of carbon atoms [1] arranged in a perfect honeycomb structure as shown in Fig. 1. 1 (a), have a host of useful properties [2]: low density, excellent mechanical stability, highly flexibility, and large specific surface area. Monolayer graphene is a zero-gap semiconductor and its conduction and valence bands cross at points K and K' (Fig. 1. 1 b) [3]. Owing to this unique electronic structure, graphene demonstrated ultra-high carrier mobility of ~200,000 cm^2/Vs at a low temperature [4]. Because graphene has high transmittance (97.7%), Young's modulus (1 TPa), and thermal stability and conductivity (3000 W/mK), graphene based electrodes have been actively studied [5].

Fig. 1. 2 shows methods of graphene fabrication. Graphene first synthesized with mechanical exfoliation methods, referred as scotch tape method [1], which obtains the high quality graphene sheet in spite of the difficulty to massively production. Chemical vapor deposition (CVD), which grows graphene on metal substrate such as Cu, is effective method to fabricate large area uniform graphene. However, this process typically requires transfer from metal support to dielectric substrate. Liquid phase exfoliation of graphite disperses expanded layers into a solvent, which is suitable for massive production [6]. Graphene oxide (GO) is synthesized by this method [7] and dispersed into water owing to its surface functional groups (Fig. 1. 3). This method, nevertheless, introduced irreversible change such as functional groups or defects on graphene sheets, and then deteriorates their properties.
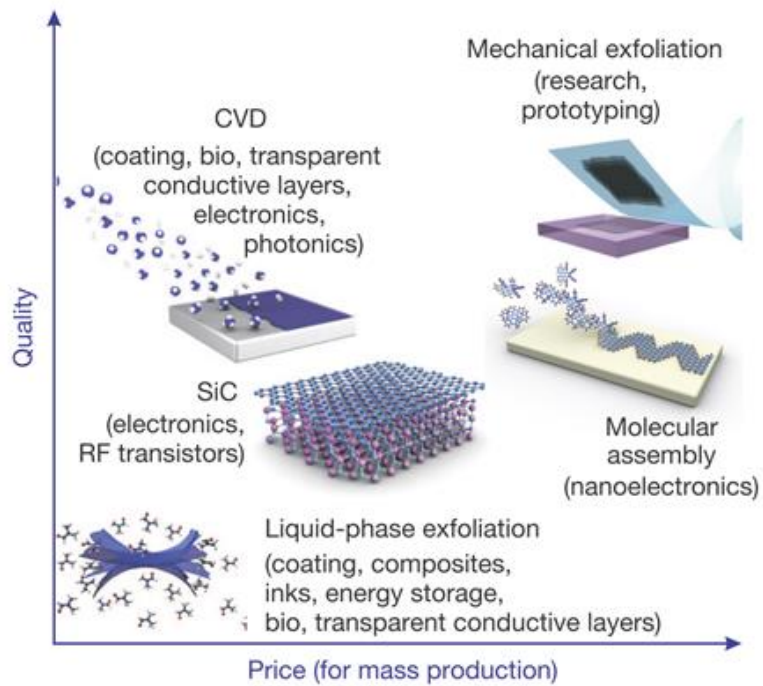
(a)

(b)

Energy   Energy

                         Conduction band

K' k_y K k_y

k_x E_F k_x E_F

                          Valence band

Fig. 1. 1 (a) Schematic graphene structure.

(b) Band structure of graphene near the Fermi level [3].

Mechanical exfoliation
(research,
prototyping)

CVD
(coating, bio, transparent
conductive layers,
electronics,
photonics)

Quality

SiC
(electronics,
RF transistors)

Molecular
assembly
(nanoelectronics)

Liquid-phase exfoliation
(coating, composites,
inks, energy storage,
bio, transparent conductive layers)

Price (for mass production)

Fig. 1. 2 Several methods of graphene fabrication [6].
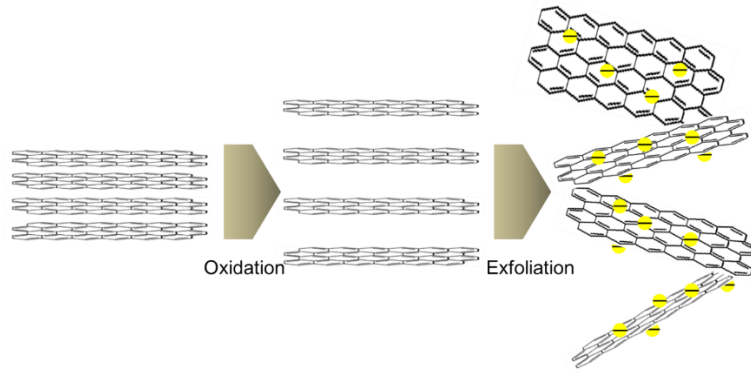
Fig. 1. 3 Preparation process of graphene oxide.

1.1.2 Graphene Oxide

Graphene have a host of useful properties, though a cost of the mechanical exfoliation and chemical vapor deposition (CVD) graphene is a problem in spite of its quality. On the other hand, graphene oxide (GO), an oxidized form of graphene, is also an atomic layer material and has various functional groups. GO is a rather promising material because of its suitability for mass production and for handling in solution process. As synthesized GO is an insulator material because functional groups disordered sp^2 graphene lattice. With reduction process such as thermal annealing, reduced GO (RGO) can partially recover its conductivity but residual damages still deteriorate the GO properties as shown in Fig. 1. 4. On the other hand, the functional groups in GO can be utilized for the functional materials. Previous study reported that functional groups facilitate low threshold field emission [8], alkylsilane functionalization [9], and proton conductivity [10]. As prepared GO is an insulator because its sp^2 lattice is disordered by functional groups. If specific kinds of functional groups are selectively removed, GO could have both protonic and electrical conductivity.

Various methods, such as thermal, chemical, and plasma treatment, are used for surface modification of GO sheets. Depending on the temperature and gas species, plasma treatment can be applied to various purposes: reducing surface layers [11], repairing defects [12], etching sheets [13], and doping heteroatoms [14, 16, 18]. Different from conventional doping methods requiring highly temperature above 300°C [15, 17], the plasma treatment can be used at room temperature and expected to have unique effects for the reduction and doping. In recent years, nitrogen doped graphene has been studied

widely for industrial applications. However, the structure and processes of the plasma treated GO have been unclear because of insufficient analysis of functional groups.
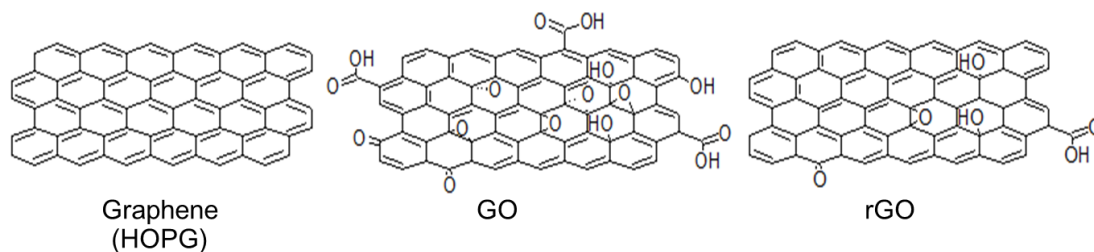
Fig. 1. 4 Schematic structure of graphene (HOPG), GO, and RGO

1.1.3 Surface Modification of Graphene

Doping of heteroatoms is one of the promising methods to tailor the electronic properties of graphene for achieving various industrial applications. Nitrogen-doped graphene has been investigated widely as the potential candidates of catalyst for fuel cell oxygen reduction reaction [19], anode materials of lithium-ion batteries [20], electrodes of bio-sensors [14], and ultracapacitors [21], etc. In these applications, doped nitrogen enhances these performances and the difference of doping site is important for the device performance. Because previous studies doped nitrogen at various sites and in various amounts, relations between doping sites and doping effects are unclear, especially on the basis of electronic structures, due to difficulty of controlling doping sites.

Synthesis of N-doped graphene has been carried out mostly by direct growth or post treatment. The direct growth is performed by chemical vapor deposition (CVD) [22-25], pyrolysis [26], arc-discharge [27], etc. using carbon and nitrogen atom containing molecules. The post treatment is, on the other hand, carried out to graphene, graphene oxide, and graphite via heating in nitrogen containing gases [15,28], plasma treatment [14,21,29,30], ion bombardment [31,32], etc. In the former case, the properties of grown product such as crystallinity, grain size, nitrogen content, etc. are often affected strongly by the preparation process. In the latter case, when we use highly oriented pyrolytic graphite (HOPG), we could reproducibly prepare a well-defined substrate to which nitrogen doping will be conducted by post treatment.

1.1.4 Controlling Work Function

Graphene is one of the most attractive electrode materials owing to its excellent optical transparency, mechanical strength, and electrical conductivity. Work function engineering can enhance a graphene usability. A large injection barrier, energy gap between work function of electrodes and energy level of semiconductor, increases contact resistance and degrades its carrier mobility. In general, therefore, Au electrode, which have large work function of 5.1 eV, is typically used for p-type semiconductors, and Al electrodes, which have small work function of 4.2 eV, is used for n-type one. Especially, electrodes having extremely small work function such as Ca (2.9 eV) can enhance n-type characteristics even on pentacene [33, 34], which is generally used as p-type semiconductor. However, atmospheric instability of Ca is a problem.

Graphene has relatively large work function (4.5 eV), so that graphene electrodes is usually applied to p-type semiconductors [35]. If the work function of graphene drastically decreased, graphene could be used as electrodes for n-type semiconductors like the Ca electrodes. Furthermore, a graphene with lower work function could be used as a promising field emitter, because its atomically thin nature enhances the emitting current [36]. Various methods of tuning graphene work function are reported: using doping hetero atoms [25], functionalization [9], and applying gate voltage. In these methods, nevertheless, ranges of work function modulation were small, and lowering work function is especially difficult. On the other hand, studies using alkali metal achieved much lower work function on graphene. Cs/O dipole layer coated graphene surface and decreased its work function to 3.4 eV with solution process [38], and 1.3 eV with vacuum evaporation [39].

There have been many reports about decreasing work function of carbon materials. Especially, hydrogenation of diamond leads to a negative electron affinity surface, and decreases its work function to 3.5 eV [40, 41]. However, low carrier concentration of the diamond restricts its conductivity and precludes the application to electrodes.

1.1.5   Electrode for OFET

Graphene has been paid much attention in various research fields because of its superior electronic, mechanical, optical and thermal properties. Graphene based electrodes have been applied in a broad range of applications, such as in light emitting diodes, photovoltaic cells, and organic field effect transistors (OFETs). Several factors affect FET performance such as interfacial contact between the semiconducting layer and source/drain (S/D) electrodes [42]. The lowest unoccupied molecular orbital (LUMO) and highest occupied molecular orbital (HOMO) of organic semiconductor such as pentacene and fullerene C_{60}, and conduction band minimum (CBM) and valence band maximum (VBM) of Si are shown in left side of Fig. 1. 5. On the other hand, work functions of typical electrode materials are shown in right side of Fig. 1. 5. The efficient injection of charge carriers into the organic semiconductor can be performed by optimizing the energy gap between the energy level of organic semiconductor and work function of the graphene electrodes [35]. Sung reported that decreasing work function of S/D electrodes improved C_{60} OFETs characteristics as shown in Fig. 1. 6 [43].
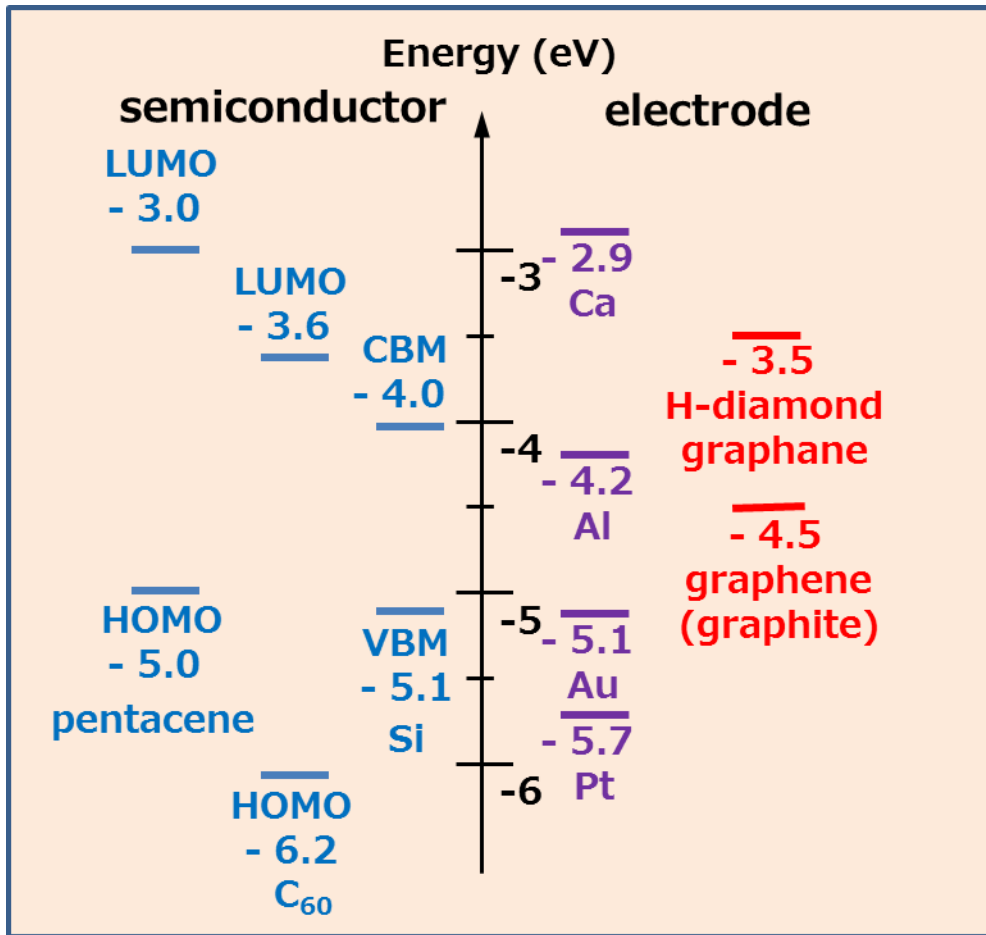
Fig. 1. 5 Energy levels of semiconductor materials and work functions of electrode materials.
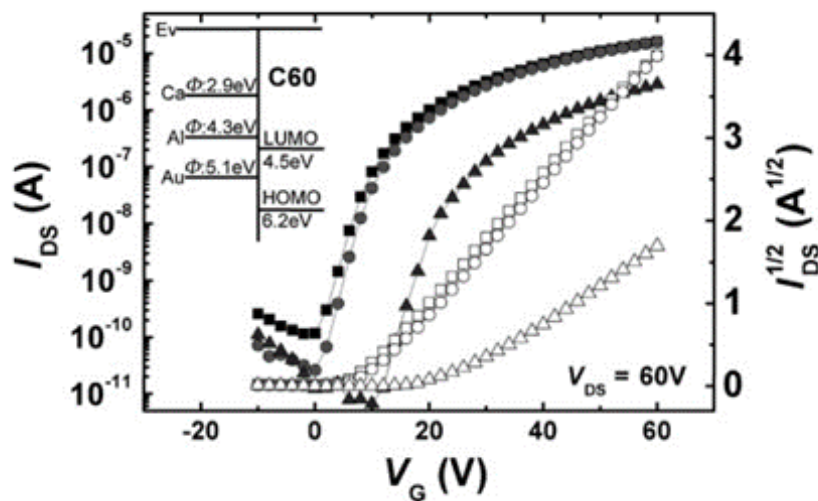

Fig. 1. 6 Typical transfer characteristics of C$_{60}$ OFETs featuring Au (triangles), Al (circles), and Ca (squares) as S/D electrodes [43].

1.2   The Aim of This Thesis

In this dissertation, I report surface modification of graphene assisted by plasma process, which leads to work function engineering of graphene. Different from conventional methods, the plasma process can treat graphene without high-temperature and toxic gases. Tuning work function would enhance the applicability of graphene as the electrodes.

第４，５，６章は雑誌等で刊行予定のため非公開
５年以内に出版予定

Reference

1   Novoselov, K. S. *et al.* Electric field effect in atomically thin carbon films. *Science* **306,** 666–9 (2004).

2   Geim, A. K. & Novoselov, K. S. The rise of graphene. *Nat. Mater.* **6,** 183–191 (2007).

3   Ando, T. The electronic properties of graphene and carbon nanotubes. *NPG Asia Mater.* **1,** 17–21 (2009).

4   Du, X., Skachko, I., Barker, A. & Andrei, E. Y. Approaching ballistic transport in suspended graphene. *Nat. Nanotechnol.* **3,** 491–5 (2008).

5   Huang, X., Zeng, Z., Fan, Z., Liu, J. & Zhang, H. Graphene-based electrodes. *Adv. Mater.* **24,** 5979–6004 (2012).

6   Novoselov, K. S. *et al.* A roadmap for graphene. *Nature* **490,** 192–200 (2012).

7   M. Hirata, T. Gotou, S. Horiuchi, M. Fujiwara, and M. Ohba, Carbon **42**, 2929 (2004).

8   Yamaguchi, H. *et al.* Field emission from atomically thin edges of reduced graphene oxide. *ACS Nano* **5,** 4945–4952 (2011).

9   Kang, B., Lim, S., Lee, W. H., Jo, S. B. & Cho, K. Work-Function-Tuned Reduced Graphene Oxide via Direct Surface Functionalization as Source/Drain Electrodes in Bottom-Contact Organic Transistors. *Adv. Mater.* **25,** 5856–5862 (2013).

10 Karim, M. R. *et al.* Graphene oxide nanosheet with high proton conductivity. *J. Am. Chem. Soc.* **135,** 8097–100 (2013).

11 Eda, G. *et al.* Graphene oxide gate dielectric for graphene-based monolithic field effect transistors. *Appl. Phys. Lett.* **102,** 1–4 (2013).

12 Cheng, M. *et al.* Restoration of graphene from graphene oxide by defect repair. *Carbon N. Y.* **50,** 2581–2587 (2012).

13 Shi, Z. *et al.* Patterning graphene with zigzag edges by self-aligned anisotropic etching. *Adv. Mater.* **23,** 3061–5 (2011).

14 Wang, Y., Shao, Y., Matson, D. W., Li, J. & Lin, Y. Nitrogen-doped graphene and its application in electrochemical biosensing. *ACS Nano* **4,** 1790–1798 (2010).

15 Wang, X. *et al.* N-Doping of Graphene Through Electrothermal Reactions with Ammonia. *Science (80-.).* **324,** 768–771 (2009).

16 Kumar, N. A. *et al.* Plasma-assisted simultaneous reduction and nitrogen doping of graphene oxide nanosheets. *J. Mater. Chem. A* **1,** 4431 (2013).

17 Li, X. *et al.* Simultaneous nitrogen doping and reduction of graphene oxide. *J. Am. Chem. Soc.* **131,** 15939–15944 (2009).

18 1.   Singh, G. *et al.* Study of simultaneous reduction and nitrogen doping of graphene oxide Langmuir-Blodgett monolayer sheets by ammonia plasma treatment. *Nanotechnology* **24,** 355704 (2013).

19 Yang, Z., Nie, H., Chen, X., Chen, X. & Huang, S. Recent progress in doped carbon nanomaterials as effective cathode catalysts for fuel cell oxygen reduction reaction. *J. Power Sources* **236,** 238–249 (2013).

20 Yu, Y.-X. Can all nitrogen-doped defects improve the performance of graphene anode materials for lithium-ion batteries? *Phys. Chem. Chem. Phys.* **15,** 16819–27 (2013).

21 Jeong, H. M. *et al.* Nitrogen-doped graphene for high-performance ultracapacitors and the importance of nitrogen-doped sites at basal planes. *Nano Lett.* **11,** 2472–2477 (2011).

22 Jin, Z., Yao, J., Kittrell, C. & Tour, J. M. Large-scale growth and characterizations of nitrogen-doped monolayer graphene sheets. *ACS Nano* **5,** 4112–4117 (2011).

23 Imamura, G. & Saiki, K. Synthesis of Nitrogen-Doped Graphene on Pt(111) by Chemical Vapor Deposition. *J. Phys. Chem. C* **115,** 10000–10005 (2011)

24 Terasawa, T. & Saiki, K. Synthesis of Nitrogen-Doped Graphene by Plasma-Enhanced Chemical Vapor Deposition. *Jpn. J. Appl. Phys.* **51,** 055101 (2012).

25   Schiros, T. *et al.* Connecting dopant bond type with electronic structure in N-doped graphene. *Nano Lett.* **12,** 4025–31 (2012).

26   Sun, Z. *et al.* Growth of graphene from solid carbon sources. *Nature* **468,** 549–52 (2010).

27   Panchakarla, L. S. *et al.* Synthesis, Structure, and Properties of Boron- and Nitrogen-Doped Graphene. *Adv. Mater.* **21,** 4726–4730 (2009).

28   Hwang, J. O. *et al.* Workfunction-tunable, N-doped reduced graphene transparent electrodes for high-performance polymer light-emitting diodes. *ACS Nano* **6,** 159–67 (2012).

29   Lin, Y.-C., Lin, C.-Y. & Chiu, P.-W. Controllable graphene N-doping with ammonia plasma. *Appl. Phys. Lett.* **96,** 133110 (2010).

30   Shao, Y. *et al.* Nitrogen-doped graphene and its electrochemical applications. *J. Mater. Chem.* **20,** 7491 (2010).

31   Kondo, T. *et al.* Atomic-scale characterization of nitrogen-doped graphite: Effects of dopant nitrogen on the local electronic structure of the surrounding carbon atoms. *Phys. Rev. B* **86,** 035436 (2012).

32   Zhou, Y. *et al.* Dopant-Induced Electronic Structure Modification of HOPG Surfaces: Implications for High Activity Fuel Cell Catalysts. *J. Phys. Chem. C* **114,** 506–515 (2010).

33   Takebayashi, S., Abe, S., Saiki, K. & Ueno, K. Origin of the ambipolar operation of a pentacene field-effect transistor fabricated on a poly(vinyl alcohol)-coated Ta2 O5 gate dielectric with Au source/drain electrodes. *Appl. Phys. Lett.* **94,** 5–8 (2009).

34   Yasuda, T., Goto, T., Fujita, K. & Tsutsui, T. Ambipolar pentacene field-effect transistors with calcium source-drain electrodes. *Appl. Phys. Lett.* **85,** 2098–2100 (2004).

35   Lee, S. *et al.* Enhanced charge injection in pentacene field-effect transistors with graphene electrodes. *Adv. Mater.* **23,** 100–5 (2011).

36   Yamaguchi, H. *et al.* Field emission from atomically thin edges of reduced graphene oxide. *ACS Nano* **5,** 4945–4952 (2011).

37   Yu, Y.-J. *et al.* Tuning the graphene work function by electric field effect. *Nano Lett.* **9,** 3430–4 (2009).

38   Huang, J.-H., Fang, J.-H., Liu, C.-C. & Chu, C.-W. Effective work function modulation of graphene/carbon nanotube composite films as transparent cathodes for organic optoelectronics. *ACS Nano* **5,** 6262–71 (2011).

39   Yuan, H. *et al.* Engineering Ultra-Low Work Function of Graphene. *Nano Lett.* **15,** 6475–6480 (2015).

40   Cui, J., Ristein, J. & Ley, L. Electron Affinity of the Bare and Hydrogen Covered Single Crystal Diamond (111) Surface. *Phys. Rev. Lett.* **81,** 429–432 (1998).

41   Okano, K., Koizumi, S., Silva, S. R. P. & Amaratunga, G. A. J. Low-threshold cold cathodes made of nitrogen-doped chemical-vapour-deposited diamond. *Nature* **381,** 140–141 (1996).

42   Kang, B., Lim, S., Lee, W. H., Jo, S. B. & Cho, K. Work-Function-Tuned Reduced Graphene Oxide via Direct Surface Functionalization as Source/Drain Electrodes in Bottom-Contact Organic Transistors. *Adv. Mater.* **25,** 5856–5862 (2013).

43   Sung, C.-F. *et al.* Flexible fullerene field-effect transistors fabricated through solution processing. *Adv. Mater.* **21,** 4845–9 (2009).

Chapter 2
Experimental Equipment

2.1　Fabrication and Measurement System

　　　Fig. 2. 1 shows an *in situ* vacuum system and Fig. 2. 2 shows a picture of sample preparation chamber and analysis chamber. The sample preparation chamber (1×10^{-6} Pa base pressure) is used for plasma treatment and IR-lamp annealing (THERMO RIKO, GVL298). The capacitively coupled plasma (CCP) is generated between two electrodes in this chamber (EIKO, ES-230). The upper electrode with the sample on is grounded and the other one is connected to the radio frequency (RF) power supply of 13.56 MHz [1]. Fig. 2. 3 shows pictures of nitrogen, argon, and hydrogen plasma. The prepared sample was transferred into the analysis chamber (1×10^{-7} Pa base pressure) without breaking vacuum for X-ray photoelectron spectroscopy (XPS) and Ultraviolet photoelectron spectroscopy (UPS). In addition, C_{60} deposition chamber (1×10^{-5} Pa base pressure) was connected to analysis chamber to form an organic molecular membrane.
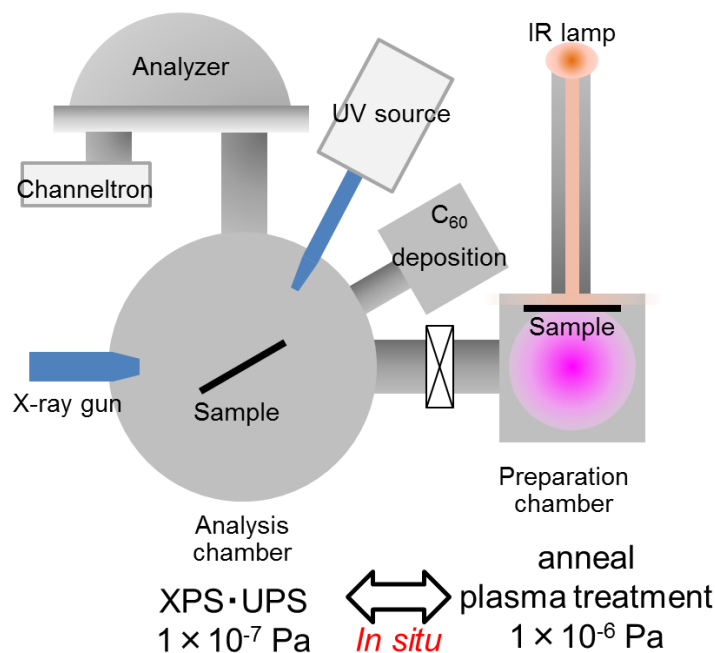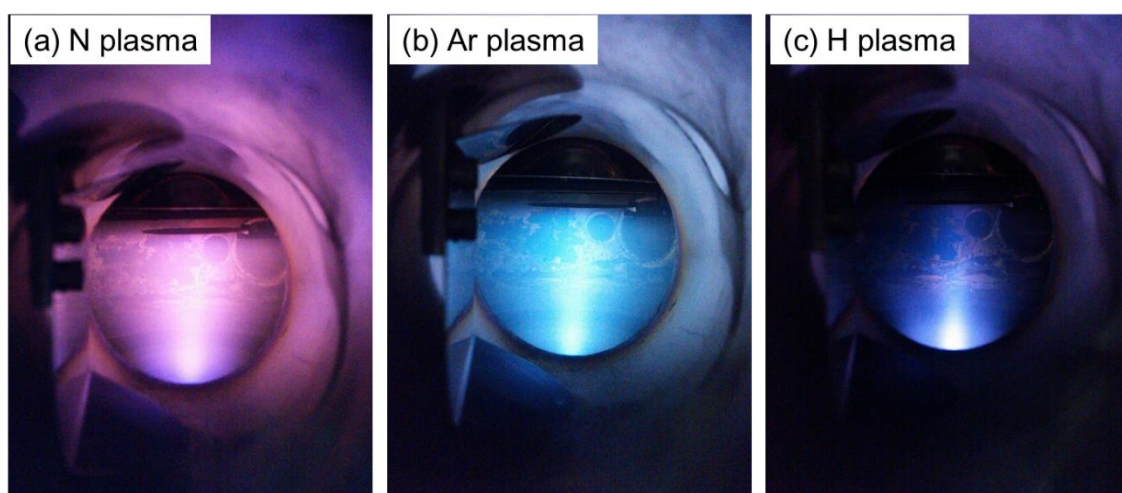

Fig. 2. 1 Schematic illustration of experimental apparatus.
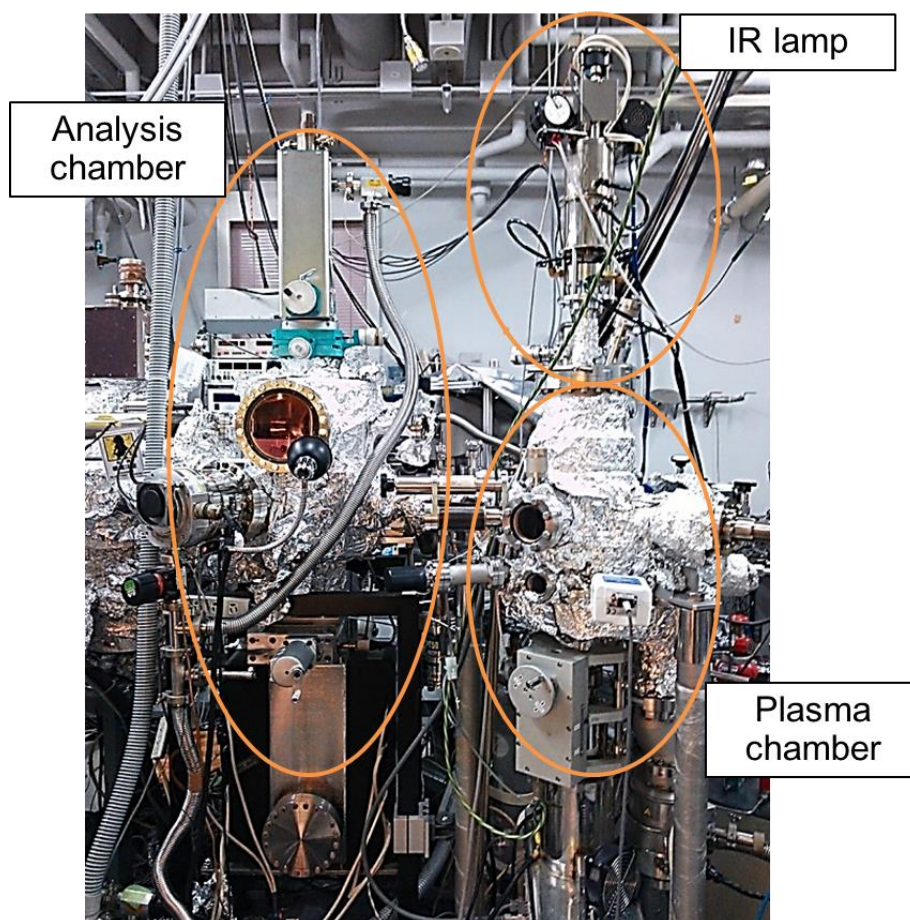
Fig. 2. 2 Picture of Analysis and plasma chamber.

**Fig. 2. 3 Pictures of nitrogen (a), argon (b), and hydrogen plasma
in plasma chamber.**

## 2.2　Photoelectron Spectroscopy

　　　X-ray photoelectron spectroscopy (XPS), a surface sensitive quantitative spectroscopic technique, is the most widely used for measuring the element composition of the sample. On the other hand, ultraviolet photoelectron spectroscopy (UPS), a surface spectroscopic technique same as XPS, is used for measuring valence band spectrum and work function. The XPS and UPS equipment is shown in Fig. 2. 4. XPS spectra are obtained by irradiating a sample surface with an Mg Kα ($h\nu$ = 1253.6 eV) X-ray light source (Thermo VG Scientific, XR3E2) and UPS spectra is obtained with monochromatized He I ($h\nu$ = 21.2 eV) light source (SPECS, UVS300). The kinetic energies of the emitted photoelectrons are measured with hemispherical analyzer (SPECS, HSA 3500). The electron binding energy E_b is determined by below equation:

$$E_b = h\nu - E_k - \phi$$

where h is the Planck's constant, ν is the frequency of the incident photon, E_k is the kinetic energy, and ϕ is the work function of the sample. The work function determined by UPS is given by

$$\phi = h\nu - E_{cutoff}$$

where E_{cutoff} is the binding energy at the secondary electron energy cutoff as shown in Fig. 2. 5. The work function was measured with a sample bias to accelerate low energy secondary electrons. Fig. 2. 6 shows UPS spectra near the energy cutoff with sample bias of -3 eV, -5 eV, and -7 eV. In the case of -3 eV, the energy cutoff was unclear because of the low acceleration. In the case of -7 eV, on the other hand, energy cutoff occasionally became stepwise possibly because excessive bias voltage mixed other peaks coming from outside of the sample. For these reasons, I applied sample bias of -5 eV for measuring work function in this study.
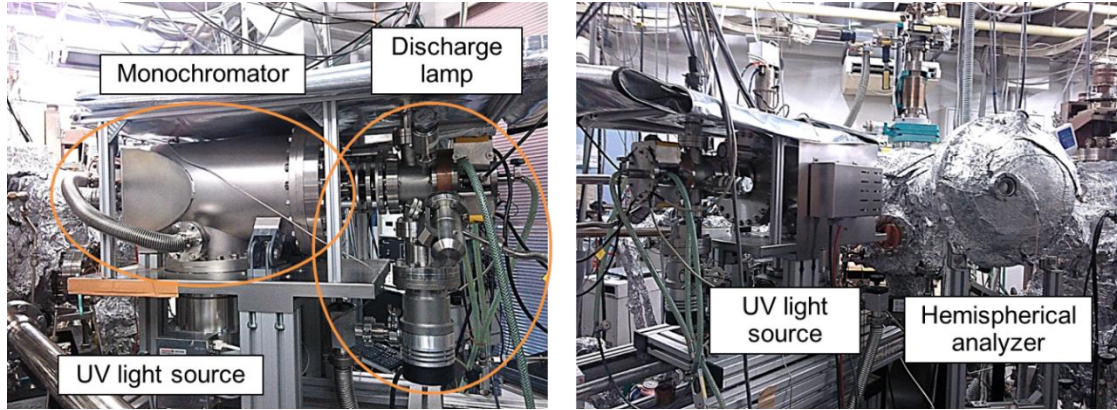
Fig. 2. 4 Pictures of UV light source and Hemispherical analyzer
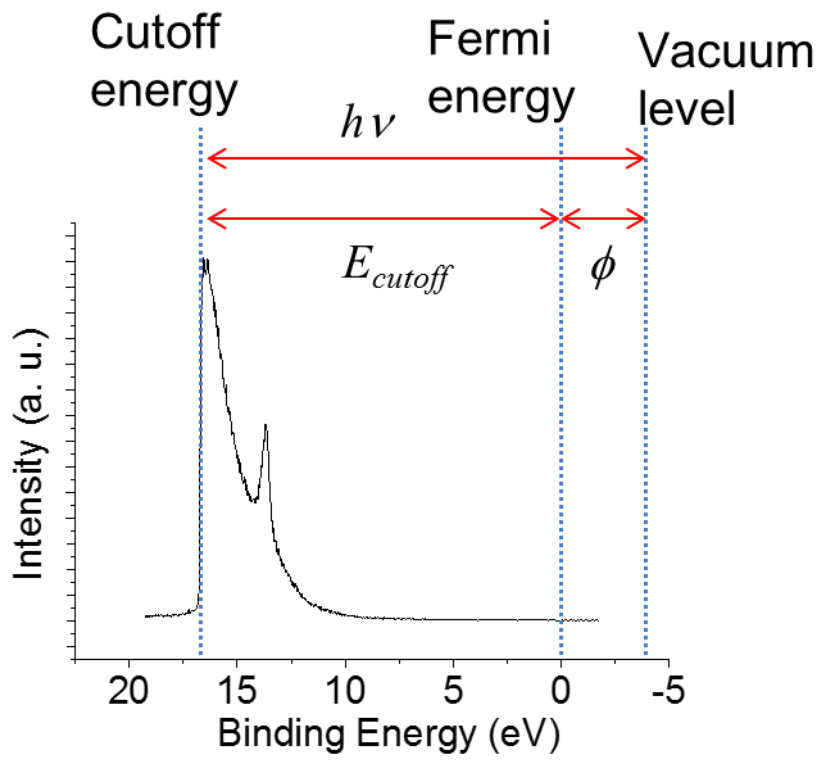
**Fig. 2. 5 UPS spectra from HOPG with sample bias to -5 eV.**
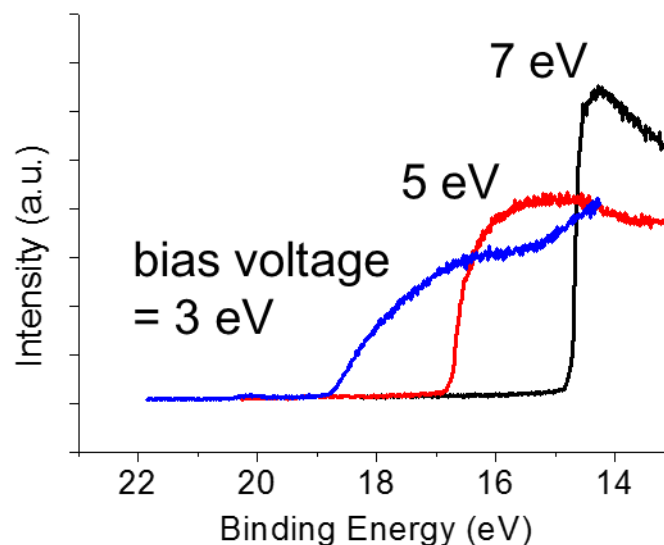
**Fig. 2. 6 UPS spectra from Si (100) with various sample bias.**

2.3 Field Effect Transistor

A schematic illustration of C_{60} organic field effect transistor (OFET) fabricated in this study is shown in Fig. 2. 7 with a thickness of each layer. OFETs, which operate as a capacitor, consist of semiconductor layer (C_{60}), insulator layer (SiO_2), gate electrode (Si), and source/drain (S/D) electrodes (RGO). The architecture of OFETs are mainly classified into top and bottom contact configurations by whether S/D electrodes locate below or above semiconductor layer. In this study, RGO sheets were used as bottom contact S/D electrodes. Spin-coater (KYOWARIKEN, K-359SD-1), shown in Fig. 2. 8 (a), forms GO electrodes uniformly. To estimate a carrier mobility of measured device, channel width and length between the electrodes are determined with optical microscope (KEYENCE, VH-Z500R) shown in Fig. 2. 8 (b). Fig. 2. 9 shows an equipment for FET measurement. The source and drain electrodes on a sample are electrically connected with Au wires, and gate voltage is applied to the sample stage. For removing oxygen and water adsorption, samples were annealed in FET chamber with W heater introduced under the sample stage.
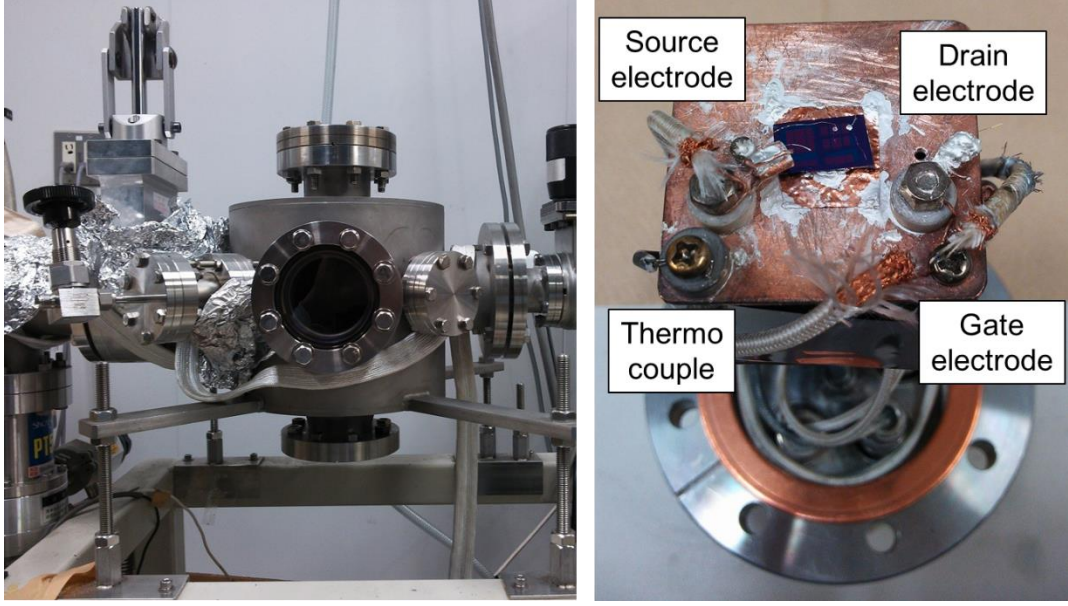
17
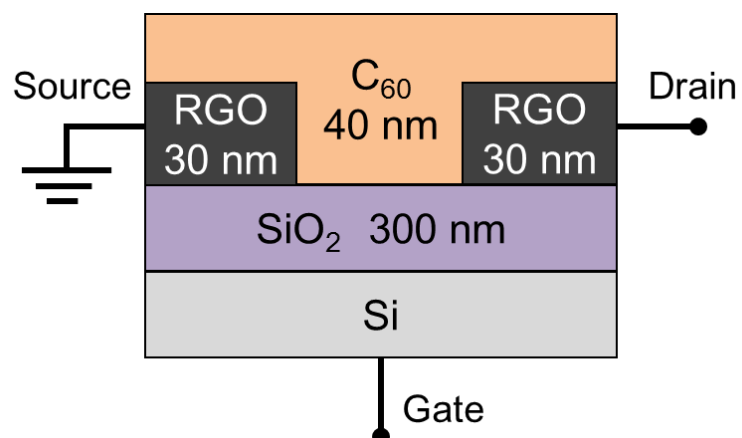
Fig. 2. 7 Schematic cross section of C60 OFET device.
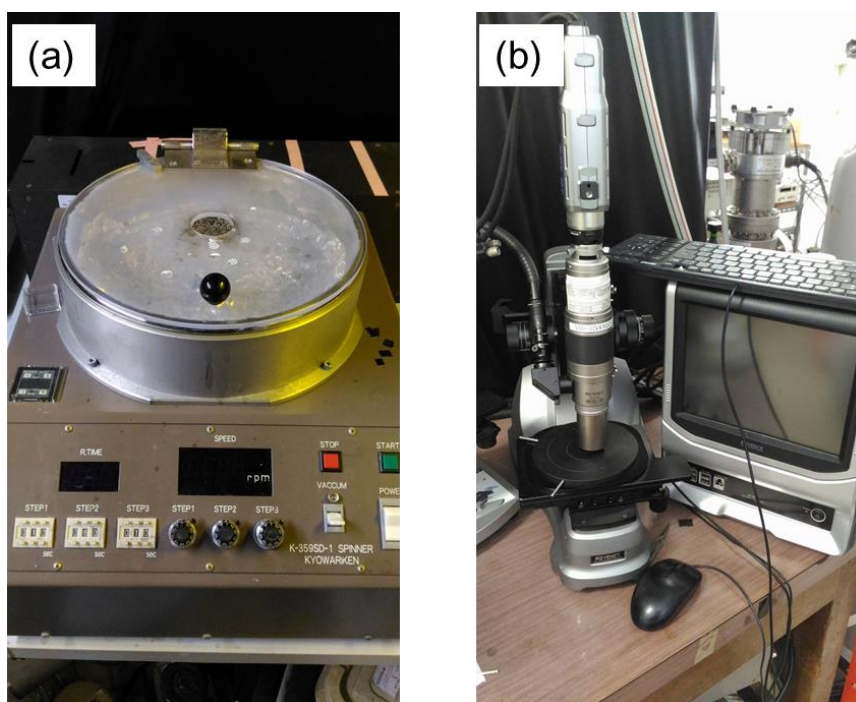
Fig. 2. 8 Equipment of spin-coater (a) and optical microscope (b).

Fig. 2. 9 Pictures of chamber and sample stage for FET measurement.

In the n-type OFET, such as C_{60} OFET, a positive V_G accumulates electron carriers at the interface between semiconductor and insulator. When V_G is higher than threshold voltage V_T, the amount of induced carriers is proportional to V_G -V_T and the capacitance Ci. Fig. 2. 10 (a) shows a typical OFET output curves, plot of source-drain current I_{SD} as a function of source-drain voltage V_{SD}. When a small V_{SD} is applied, the I_{SD} flowing channel is proportional to V_{SD}. When V_{SD} increased, the channel is pinched off at a point of $V_{DS} = V_G - V_{TH}$, because the strong V_{SD} cancelled V_G and formed a depletion region. Further increasing the V_{SD} leads only to an expansion of the depletion region and saturates I_{SD} [2].

Fig. 2. 10 (b) shows a transfer characteristics obtained from saturation region in the Fig. 2. 10 (a). The field-effect mobility (μ) and V_T was extracted from the transfer curve with the standard current-voltage equation for a transistor in the saturation regime:

$$I_{SD} = (WC_i/2L)\mu(V_G-V_T)^2$$

where I_{SD} is the saturated drain current, W is the transistor channel width, L is the transistor channel length, and Ci is the capacitance per unit area of gate insulator.
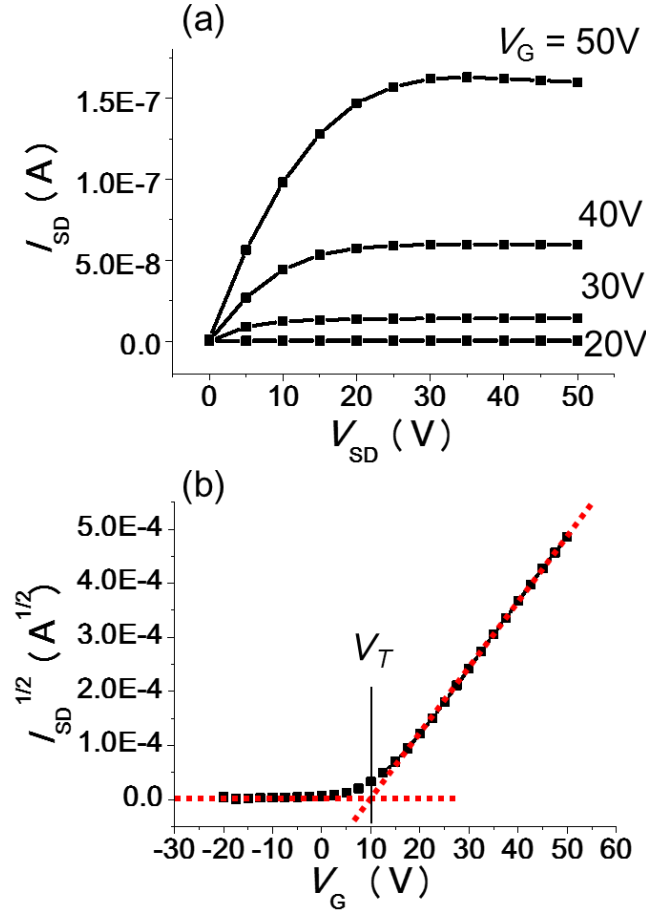
Fig. 2. 10 Typical n-type FET output (a) and transfer (b) characteristics.

2.4   Raman Spectroscopy

Raman spectroscopy exploits a phenomenon of Raman scattering, the inelastic scattering of photons by phonons. Fig. 2. 11 shows a picture of Raman spectroscopy equipment (JASCO, NRS-3100). Different from Rayleigh scattering (elastic scattering), in which the frequency of the emitted photon remains the same as the incident one, the emitted photon can lose or gain part of its energy in the inelastic process of Raman scattering. These scattering process, Stokes and Anti-Stokes process, are plotted as the intensity of the scattered light as a function of the difference of wavenumber between incident and scattered photon (Raman shift) [3]. Raman spectroscopy is used to determine the number of layers, quality of lattice structure, and the effect of perturbations such as

electric and magnetic fields, strain, doping, disorder and functional groups of sp^2 carbon materials. In particular, graphene is suitable for Raman techniques because the zero gap band structure makes all wavelength of incident light resonant.

The Raman spectrum of graphene layer consists of distinct bands. Fig. 2. 12 shows the spectra of exfoliated graphene, pristine-HOPG, damaged-HOPG, and GO samples. The peak at ~ 1580 cm^{-1} is called G peak, which corresponds E_{2g} phonon. This peak widely observed in sp^2 lattice structure. The peak at ~ 1350 cm^{-1} is called D peak, originated from the breathing modes of six-atom rings, and requires a defect for activation. The 2D peak at ~ 2700 cm^{-1} is the D peak overtone, but no defects are required for its activation. The intensities of G and D, peaks reflect quantity of graphene lattice and amount of defects, respectively. The intensity and shape of 2D peak correlates quality of graphene layers. Different from sharp 2D peak in clean single layer graphene, 2D band in HOPG consist of two peaks, $2D_1$ (higher main peak) and $2D_2$ (lower shoulder peak). This is explained by the splitting of π electron dispersion energies caused by the neighboring graphene interaction [4]. GO sample has typical weak 2D peak and D + D' defect-activated peak near 2950 cm^{-1}.

Damaged graphite classified into three stages by the disorder amount: stage 1: graphite to nanocrystalline graphite; stage 2: nanocrystalline graphite to low sp^3 amorphous carbon; stage 3: low sp^3 amorphous carbon to high sp^3 amorphous carbon. In stage 1, the crystal size L_a can be estimated with ratio of D and G peak intensities as:

$$I(D)/I(G) = C(\lambda)/L_a$$

where coefficient $C(\lambda) = 2.4 \times 10^{-10} \lambda^4$, λ is the excitation wavelength, and $I(D)$ and $I(G)$ are intensities of D and G peaks [5]. This relationship is valid when La is above ~ 2 nm. As disorder increases, $I(D)/I(G)$ saturates and then turn to decrease. In stage 2, L_a is estimated by new relation as,
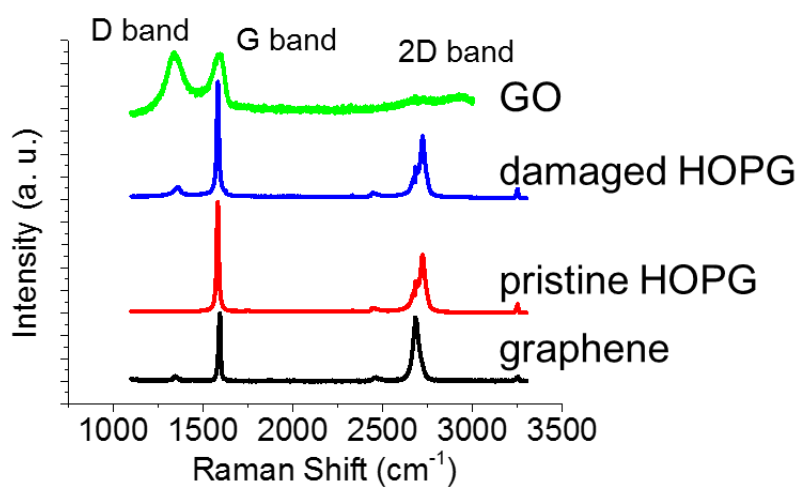
$$I(D)/I(G) = C'(\lambda)L_a^2$$

$C'(\lambda)$ can be determined with imposing continuity between stage 1 and stage 2. Because

21

GO has highly disordered graphene structure like stage 2, I(D)/I(G) ratio of GO remain nearly constant or slightly increased after reduction [6].

Fig. 2. 11 Measurement system for Raman spectroscopy.

Fig. 2. 12 Typical Raman spectra of graphene, pristine HOPG, damaged HOPG and GO.

Reference

1   Terasawa, T. & Saiki, K. Growth of graphene on Cu by plasma enhanced chemical vapor deposition. Carbon N. Y. 50, 869-874 (2012).

2   Zaumseil, J. & Sirringhaus, H. Electron and ambipolar transport in organic field-effect transistors. *Chem. Rev.* **107,** 1296–1323 (2007).

3   Ferrari, A. & Basko, D. Raman spectroscopy as a versatile tool for studying the properties of graphene. *Nat. Nanotechnol.* **8,** 235–46 (2013).

4   Kaniyoor, A. & Ramaprabhu, S. A Raman spectroscopic investigation of graphite oxide derived graphene. *AIP Adv.* **2,** 032183 (2012).

5   Ferrari, A. C. Raman spectroscopy of graphene and graphite: Disorder, electron-phonon coupling, doping and nonadiabatic effects. *Solid State Commun.* **143,** 47–57 (2007).

6   Eda, G. & Chhowalla, M. Chemically derived graphene oxide: Towards large-area thin-film electronics and optoelectronics. *Adv. Mater.* **22,** 2392–2415 (2010).

Chapter 3
Nitrogen Doping to Graphene

3.1 Introduction

Synthesis of N-doped graphene has been carried out by various methods. Chemical vapor deposition (CVD) [1,2,3,4] grows N-doped graphene by adding nitrogen sources (ammonia, pyridine etc.) into the carbon source. Thermal reaction method is heating graphene in nitrogen containing gases such as ammonia [5]. Chemical treatments use reaction with graphene and nitrogen sources such as hydrazine. In this dissertation, I have synthesized nitrogen-doped graphene by using plasma treatment [6,7,8,9], which has several advantages as compared with conventional chemical treatment: usability of safer gases, decrease in substrate temperature, etc. By appropriate pre-treatment, we could prepare the HOPG substrate of the same initial state, which assures experimental reproducibility. We have prepared two kinds of substrates: one was pristine HOPG (p-HOPG) with large grains and the other was damaged HOPG (d-HOPG) which had been exposed to Ar plasma. Nitrogen doping was carried out to both p-HOPG and d-HOPG. Comparing the results on these samples, we could elucidate the relation between the doping site and the work function. These findings would open a way to control the doping site and tune the work function of graphene.

3.2 Experimental Method

A p-HOPG sample was obtained by cleaving the surface of a HOPG crystal in air and annealing at 700°C for 1 hour under a vacuum of 1×10^{-5} Pa. The *in situ* X-ray photoelectron spectroscopy (XPS) indicated no trace of impurities such as oxygen, nitrogen, etc. (Fig. 3. 1 black line). The *ex situ* Raman spectroscopy showed no trace of D band, meaning the large grain size. A d-HOPG sample was obtained by exposing p-HOPG to Ar plasma generated by RF of 10 W and the back pressure of 0.3 Pa for 1 h. After the Ar plasma treatment, the sample was annealed for 1 h in vacuum for degassing

and curing, and then cleanness of d-HOPG surface was ensured as shown in Fig. 3. 1 green line. Nitrogen plasma treatment on p-HOPG and d-HOPG samples (Fig. 3. 1 red and blue line, respectively) was carried out under the following condition: N_2 gas pressure of 0.1 Pa, N_2 gas flow rate of 0.2 sccm, and RF power of 10 W. Sample preparation processes are shown in Fig. 3. 2.
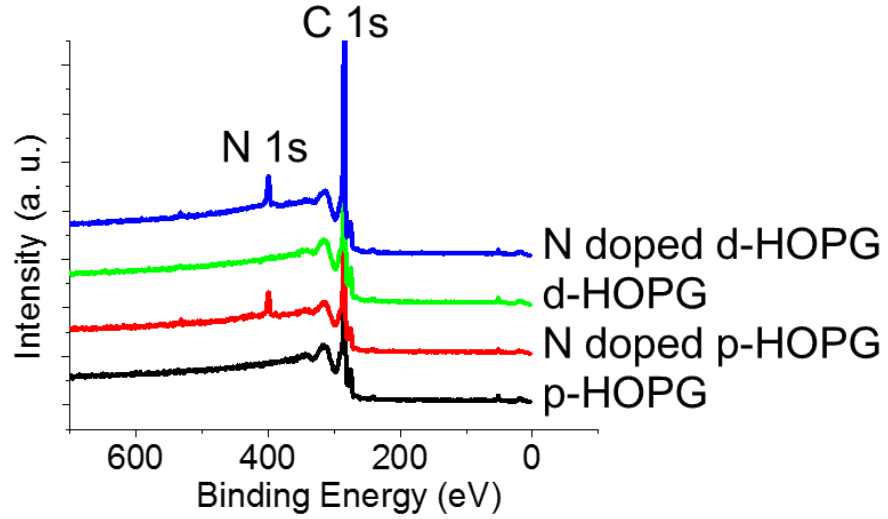

Fig. 3. 1 XPS spectra of p-HOPG before (black) and after N doping (red), and d-HOPG before (green) and after N doping (blue)
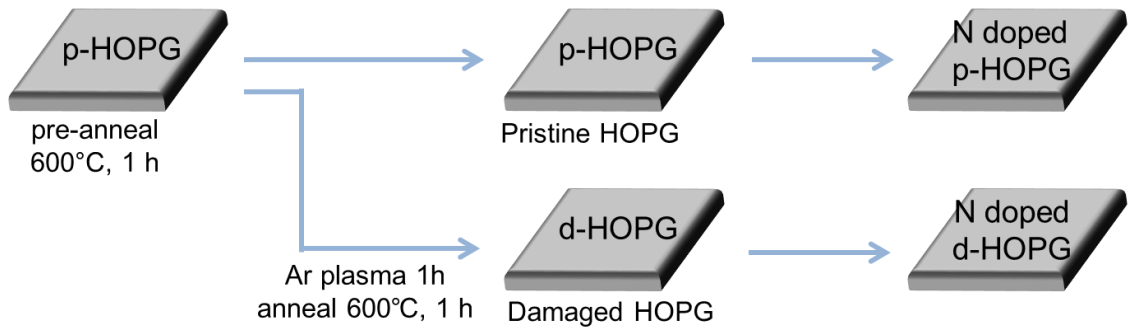

Fig. 3. 2 Sample preparation of nitrogen doped HOPG.

25

3.3   Results and Discussion

Wide range XPS spectra of HOPG samples are shown in Fig. 3. 1. The p-HOPG spectrum (black line) showed only C 1s peak from sp^2 carbon atom at binding energy of 284.5 eV. After N plasma treatment, nitrogen peak was appeared near 400 eV as shown in Fig. 3. 1 red and blue lines which were obtained after irradiation for 10 min. Fig. 3. 3 (a) shows the N 1s XPS spectra of p-HOPG samples treated by nitrogen plasma for 15 sec and 10 min, respectively. The N 1s spectral shape changes with plasma treatment time, indicative of the change in chemical state of doped nitrogen sites. The N 1s spectra were fitted into four peaks: pyridinic N (398.6 eV), pyrrolic N (399.8 eV), graphitic N (401.0 eV), and others (403.0 eV). These peaks correspond to the N atoms at the edge of six-membered ring, at the edge of five-membered ring, the substitutional site in graphene plane, and the other components, respectively (Fig. 3. 4) [9,10,11,12]. Wang *et al.* estimated that the peak component of graphitic N at the inside of a zigzag edge appears at the binding energy of 0.6 eV higher than graphitic N   [13], but such component was not observed in this study. According to the deconvolution of N 1s spectrum, the content of each component (atomic ratio to carbon) is plotted in Fig. 3. 3 (b) as a function of nitrogen plasma treatment time in a logarithmic scale. The total amounts of nitrogen were plotted as a black line together with its values. After 15 sec plasma treatment, the total nitrogen amount was 0.2%, and most of N atoms were at a graphitic site. With an increasing treatment time, the pyridinic N component increased more rapidly than the graphitic one and became comparable to the graphitic N at 2 min. Moreover, the pyrrolic N component started to rise after 2 min and then its amount became equal to that of graphitic around 10 min. Finally, the total N amount tended to saturate at approximately 9% after 10 min plasma treatment. At this stage the composition ratio also became unchanged; in order of pyridinic, pyrrolic, graphitic, and others (Fig. 3. 3).
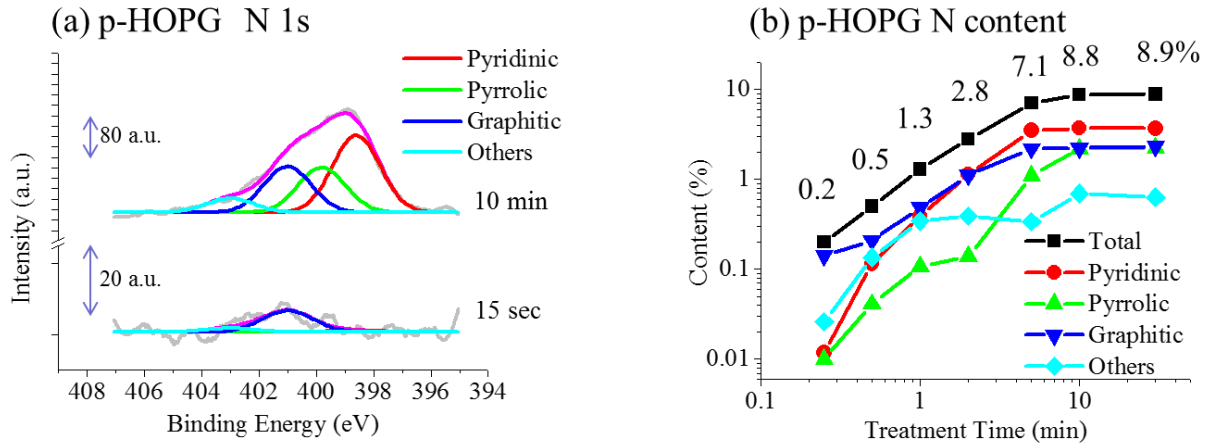
**Fig. 3. 3 N 1s XPS spectra (a) and N composition ratio as a function of treatment time (b) on p-HOPG.**
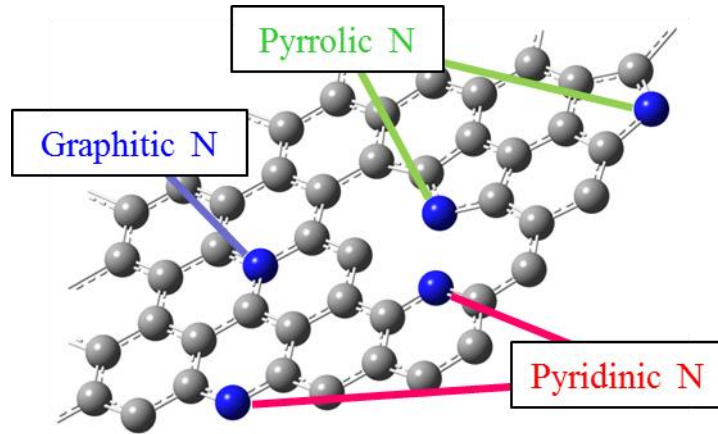
Fig. 3. 4 Typical doping sites of nitrogen in graphene lattice.

Nitrogen plasma treatment induce defects in the graphene lattice. Fujimoto and Saito calculated relation between defects and nitrogen doping. They reported substitutional doping is energetically the most favorable in non-defective graphene, but pyridinic doping becomes energetically favorable under the existence of a vacancy in graphene [14]. To estimate the amount of disorder induced by plasma treatment, I measured Raman spectra for the samples at each stage of plasma treatment.

Fig. 3. 5(a) shows the evolution of the Raman spectrum of p-HOPG samples treated by nitrogen plasma for 15 sec - 30 min. Raman spectra exhibit three main

characteristic peaks in the HOPG samples. The G band (1581 cm^{-1}), D band (1353 cm^{-1}), and 2D band (2720 cm^{-1}) are related to bond stretching of the sp^2 carbon atoms, defects, and double resonance scattering, respectively. For the untreated p-HOPG, only G and 2D peaks were observed but the D peak hardly appeared. As the nitrogen plasma treatment proceeded, the D peak started to appear and its intensity increased with an increasing treatment time. An intensity ratio of D to G peaks I_D/I_G, indicator of the amount of defects, is plotted as a function of the nitrogen plasma treatment time in Fig. 3. 5 (b).
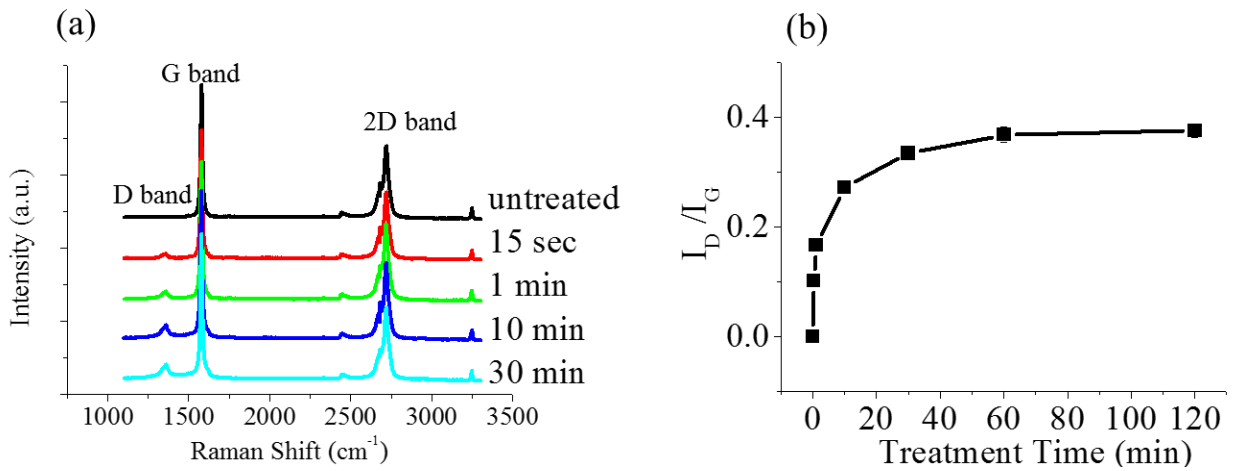

Fig. 3. 5 (a) Change of the Raman spectra with the N plasma treatment time.

(b) I_D/I_G ratio as a function of the plasma treatment time.

The I_D/I_G drastically increases with a treatment time and then saturates toward around 0.4. In the previous report [15], the I_D/I_G of HOPG first increases with the formation of defect (stage 1) and then re-decreases owing to the progress of amorphization with excessive amount of defect (stage 2). In the present case, I_D/I_G saturates and the value is much smaller than the value reported previously. Thus the surface of HOPG is remaining in the stage 1 through the whole process. This is probably because the damaged layers of HOPG surface were removed by plasma and the amount of defects reached an equilibrium state near the HOPG surface region. The peak shift of G and 2D band could not be identified.

As above, the I_D/I_G rapidly increases till 10 min, during which the component of N doping sites greatly changed (Fig. 3. 3 a). These results indicate that the defects on the

HOPG surface causes the change of N doping site. I proposed a scheme of changing doping sites depending on the surface defects in Fig. 3. 6. At the initial stage of N plasma treatment, there are small number of defective sites on graphene. Thus, doping was likely to proceed by substituting the carbon atom, which was sputtered by plasma. For this reason, doping at graphitic sites were dominant rather than at pyrrolic and pyridinic sites. As the plasma treatment proceeded, defects were formed and the edge sites on graphene were increased. Doping to the edge sites were enhanced and then the component of pyridinic and pyrrolic N doping increased (Fig. 3. 3).
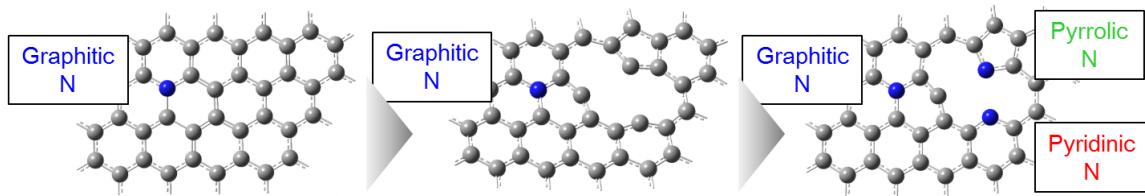
**Fig. 3. 6 Schematic process of nitrogen doping on HOPG surface.**

Based on the assumption that doping site is affected by the defects on graphene lattice, I doped nitrogen to d-HOPG sputtered by Ar plasma and compared doping sites of p- and d-HOPG. The initial I_D/I_G ratio of d-HOPG was 0.23, which compare with the p-HOPG plasma treated for 10 min (Fig. 3. 5). After the 10 min treatment, doping site of p-HOPG was changed from graphitic N dominant to pyrrolic and pyridinic N dominant. It means that initial state of d-HOPG has enough damage to change its doping sites. Fig. 3. 7 (a) shows the N 1s XPS spectra of the samples treated by nitrogen plasma for 15 sec and 10 min and Fig. 3. 7 (b) shows the change in total doping amount and content of each doped site. After nitrogen plasma treatment on the d-HOPG for 15 sec, the total doping amount was 1% which was larger than that of p-HOPG (0.2%). In addition, the pyridinic N amount was larger than the graphitic N at the early stage of plasma treatment. After 10 min plasma treatment, the composition ratio of d-HOPG was similar to that of p-HOPG, in which edge doping such as pyrrolic and pyridinic N was dominant. The d-HOPG has large amount of defects providing edge sites, and then the pyridinic N was dominant from the initial stage of plasma treatment.

(a) d-HOPG N 1s

(b) d-HOPG N content
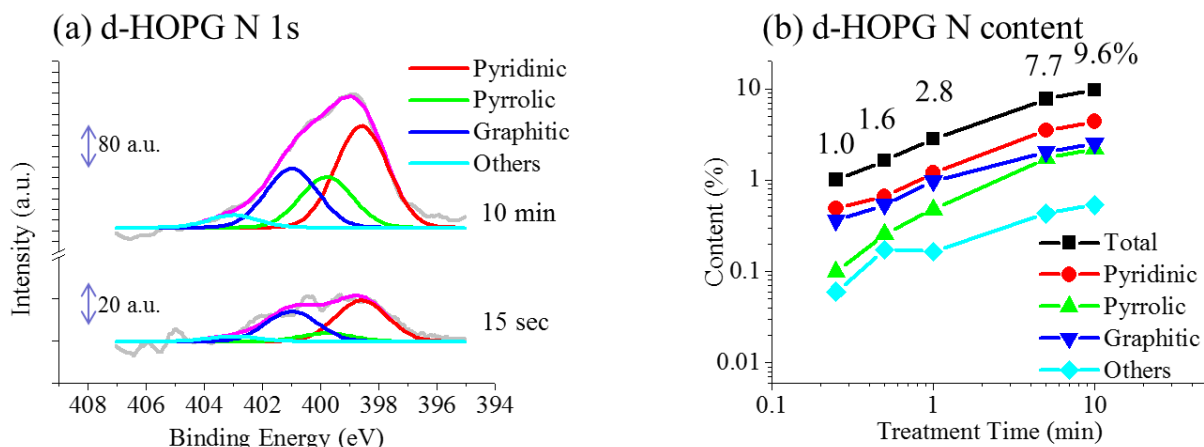
Fig. 3. 7 N 1s XPS spectra (a) and N composition ratio as a function of treatment time (b) on d-HOPG.

As above, I succeeded in controlling the nitrogen doping sites by introducing defects on HOPG surface. Next, I investigated change of electric states of doping sites by measuring work functions. Fig. 3. 8 shows the work function of p-HOPG and d-HOPG samples as a function of plasma treatment time. The work function of the untreated p-HOPG was 4.45 eV which is consistent with the values reported previous work [16,17].In the case of p-HOPG (black square line), its work function first decreased to 4.31 eV at the early stage of nitrogen plasma treatment. After 0.5 min treatment, the work function turned into a rise and saturated near 5.4 eV after 10 min treatment. As shown in Fig. 3. 3, graphitic N was dominant at the early stage of nitrogen plasma treatment and thus it can be considered that the doping at a graphitic site decreases the work function. On the other hand, the increase of work function corresponds to the becoming dominant of pyridinic N and pyrrolic N. Thus the doping to pyridinic and pyrrolic sites increases the work function.
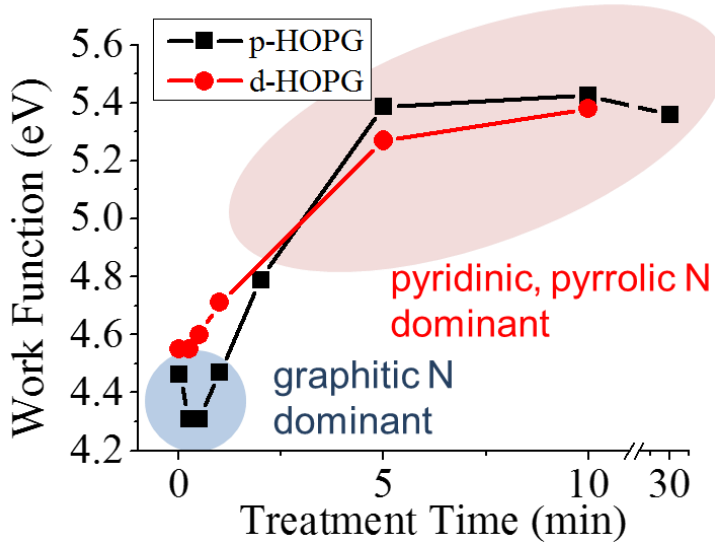
Fig. 3. 8 Change of work function of p-HOPG (black square) and d-HOPG (red circle) as a function of N plasma treatment time.

The change in work function of d-HOPG showed a different tendency as shown by a red circle line in Fig. 3. 8. The work function of d-HOPG at the initial stage (I_D/I_G = 0.23) was 4.55 eV which is 0.1 eV larger than that of the p-HOPG. The increase of work function by Ar ion irradiation has been reported in the previous work [16,17,18]. For nitrogen plasma treatment, the work function monotonically increased and reached 5.4 eV after 10 min. This is in contrast with the case of p-HOPG, in which the work function first decreases and re-increases with nitrogen plasma treatment. On d-HOPG, pyridinic and pyrrolic N were dominant from early stage of plasma treatment in different from that on p-HOPG. It seems that the dominance of pyridinic N even from the initial stage of nitrogen plasma treatment causes the monotonous increase in work function.

Based on above experimental results, I found that the nitrogen doping at a graphitic site causes the decrease in work function, while the doping at a pyridinic or pyrrolic site increases the work function. A schematic figure of change the work function is shown in Fig. 3. 9, in which band structure of graphite, typical material of semimetal, is overlapped different from single layer graphene. A work function is determined as the difference between the vacuum level and the Fermi level. Therefore, variation of density of states near the Fermi level causes the change of the work function [19, 20]. A nitrogen atom doped at a graphitic site has three σ bonds and one π bond. One nitrogen atom has five valence electrons. In the case of nitrogen atom doped at a graphitic site, part of outer electrons is transferred to the surrounding carbon atoms, since graphitic N atoms are

31

positively charged (higher binding energy in XPS). This electron donation from the graphitic N atom to the graphene lattice (electron-doping) decreases the work function. For a nitrogen atom doped at a pyridinic or a pyrrolic site, lone pair is formed at the edge nitrogen atom, resulting in negatively charged (lower binding energy in XPS) nitrogen atom and positively charged surrounding carbon atoms. Thus hole-doping occurs at graphene lattice and increases the work function [4, 18, 21, 22].
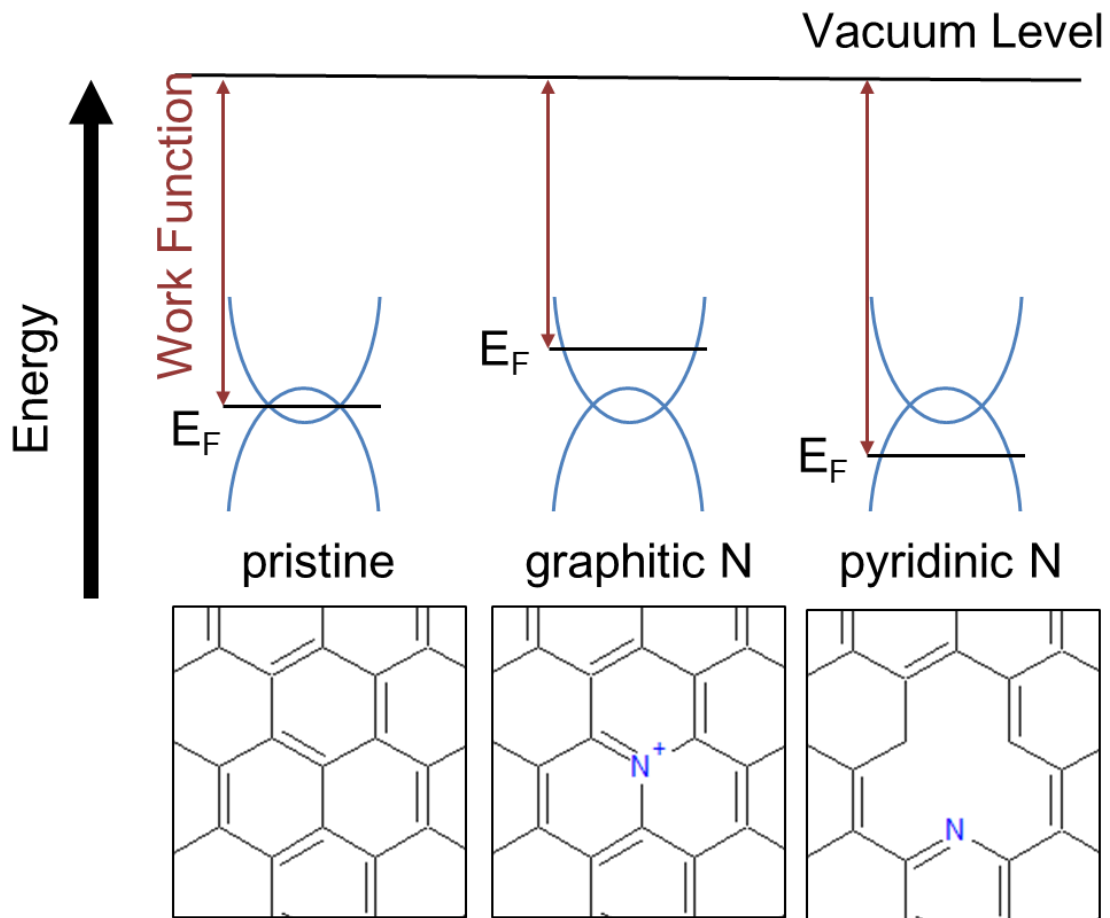
Fig. 3. 9 Schematic band structures near the Fermi level
**of doped graphite and corresponding doping sites.**

To understand a reason of the change of doping sites, I have focused on the damage from plasma treatment. For incident ions with a kinetic energy E_k that result in a C atom recoil with kinetic energy equal to the threshold energy for displacement E_d is obtained by

$$E_d = E_k \left(\frac{4m_1 m_2}{(m_1 + M_2)^2} \right)$$

where m_1 and m_2 are the masses of the two atoms involved. In the case of graphene, ^{14}N atom needs E_k of 22.04 eV for displacement of ^{12}C atom, but N can be doped when the incident ionic species are reactive and N^+ ion incorporates into pyridinic N site. Moreover, additional energy needs for the ion remaining in the lattice since the cohesive energy per atom is ~7 eV [23]. A molecular dynamics (MD) simulation predicted that a doping probability of N ion exceeds 50% with the ion energy of 45 eV [24]. Cress *et al.* experimentally demonstrated purified N^+ ion having appropriate energy (30 ~ 50 eV) was doped into substitutional (graphitic) site in topmost surface layer. Below this energy region, N^+ ion forms nitrogen-adatom on surface, whereas above this energy region, N^+ ion forms single vacancy and penetrates into under layers [23]. Different from this report, unpurified ion beam contains N^+ and N_2^+ ion and the composite ion implantation introduced large amount of pyridinic N at lower ion energy (25 eV). These results suggested that N_2^+ ion tends to introduce larger amount of defects than N^+ ion introduces. Since the nitrogen plasma generally contains N_2^+ ion [25], plasma may introduce large amount of defect to graphite lattice.

Different from graphitic and pyridinic N, which are extensively studied in experimental and theoretical reports, reports concerning pyrrolic N are limited. Fig. 3. 10 (a) shows XPS N 1s spectra of N doped HOPG. As a result of plasma treatment for 30 min, a nitrogen doping amount and component ratio reached an equilibrium state. After a thermal treatment at 600° C for 1 h, the pyrrolic N component in the sample was intensively removed, which was possibly caused by a structural instability of five-membered ring of pyrrolic N in graphene lattice. This selective desorption elucidates connection between pyrrolic N component and work function. Fig. 3. 10 (b) shows a work function and N content of N doped HOPG, which were treated by N plasma and annealing repeatedly. At the initial N doped HOPG, the work function was about 5.4 eV (black line) and N content was 8.6 at% (red line). As a result of annealing, work function and N content decreased to 5.2 eV and 6.3 at%. These results strong suggest that pyridinic N

increased work function of graphene. Repeated experiment, moreover, demonstrated high reproducibility of these results.
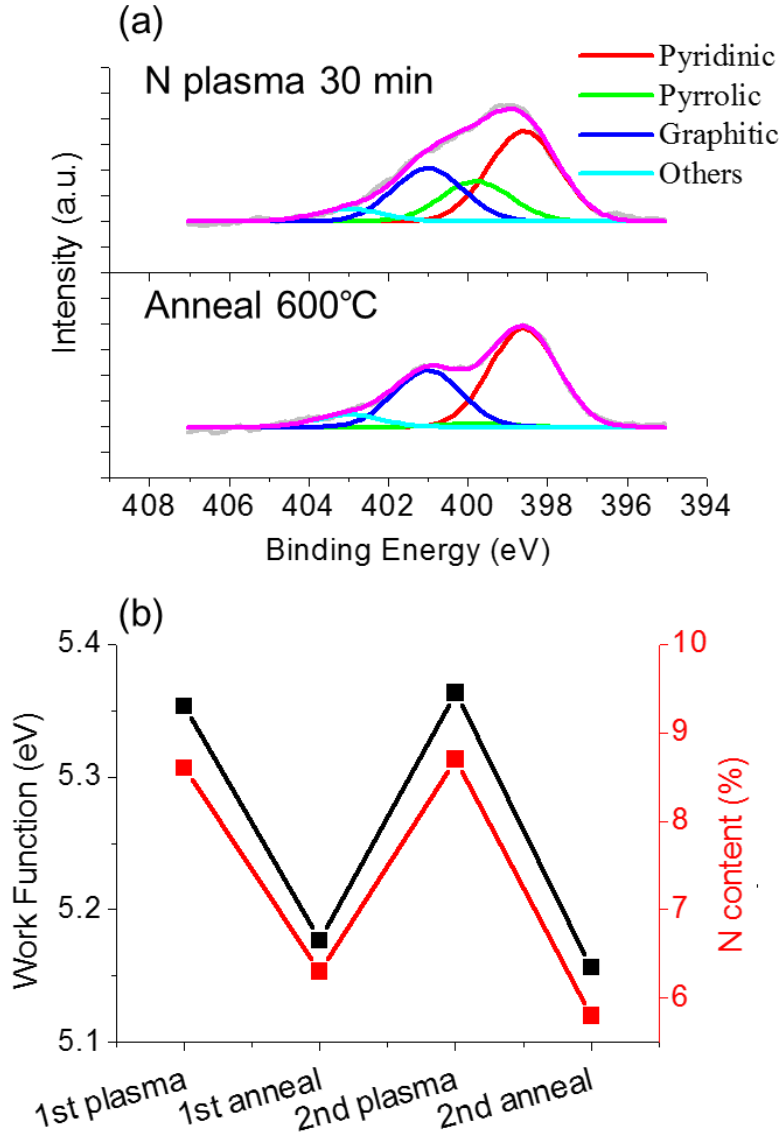
Fig. 3. 10 (a) XPS N 1s spectra of N doped HOPG before and after annealing. (b) Work function and N content of N doped HOPG after repetitive N plasma and thermal treatment.

He-I UV light source can excite only valence band electrons, which provide information about the distribution of electrons in the VB and density of state (DOS) near the Fermi level. Fig. 3. 11 (a) shows valence band spectra of HOPG samples. Pristine

HOPG (black line) shows sharp σ peak at 13.7 eV which is intrinsic to graphite. After Ar plasma treatment, defect induced peak is appeared at ~9.1 eV. N plasma treatment also induced defective peak like Ar treatment. Furthermore, N doped HOPG showed slightly N lone pair peak at ~ 4 eV in logarithmic graph in Fig. 3. 11 (b) [26]. The peak position of σ band depends on layer distance, which can be shifted by intercalation of alkali metal [27]. Almost same σ peak positions of plasma treated HOPG denied a possibility of gas intercalation between the graphite layers.
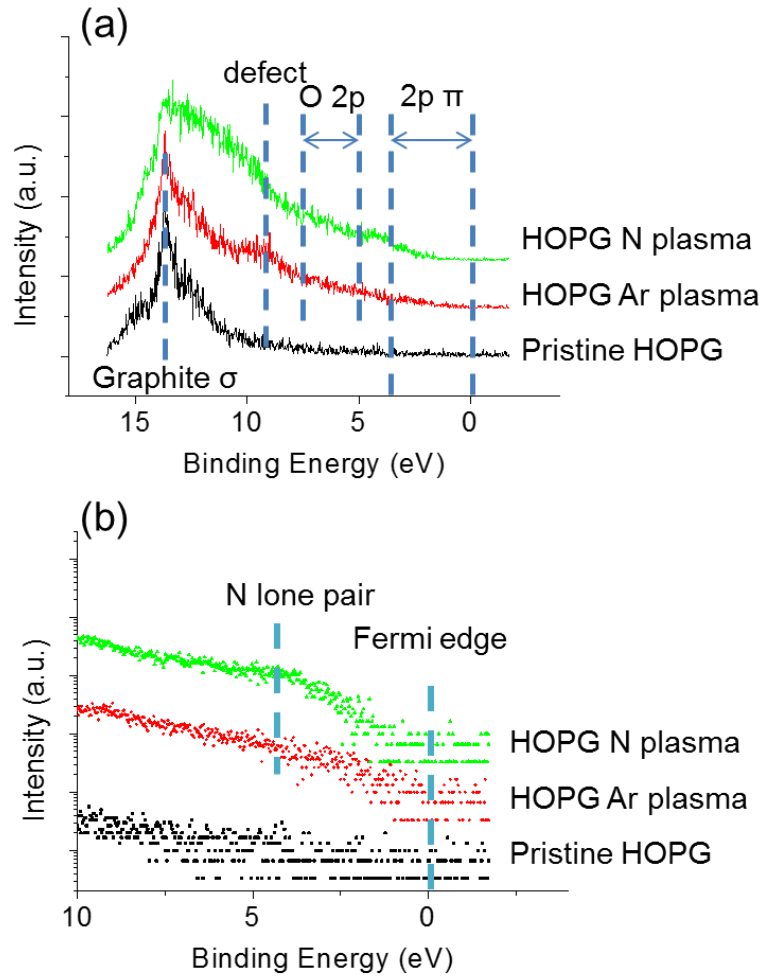

Fig. 3. 11 UPS valence band spectra of plasma treated HOPG. These spectra are plotted on a linear scale (a) and logarithmic scale near the Fermi energy (b).

Finally, to estimate the nitrogen doping depth, XPS spectra were measured at various electron emission angles. As shown in Fig. 3. 13, XPS spectra of doped HOPG

were changed depending on the angles. At lower emission angle such as 15°, C 1s spectra shows sharp peak at C-C bond (284.5 eV) and N 1s spectra shows small peak intensities. In contrast, at higher emission angle as 60°, C 1s has broader shape which has large C-N peak shoulder at higher binding energy, and N 1s peak becomes large intensity. With angle-resolved XPS (AR-XPS), the thickness of nitrogen doped carbon d can be determined by the C 1s core level intensity ratio of nitride carbon I_N and substrate carbon I_C by
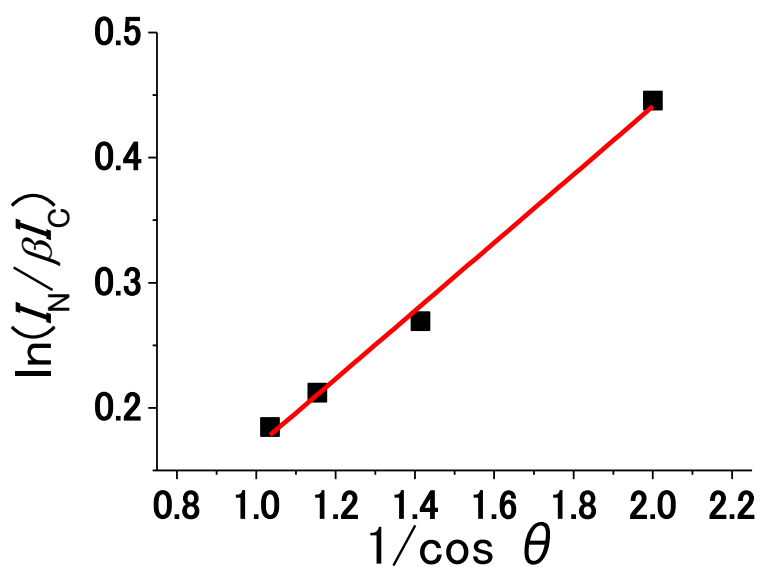
$$d = \lambda \cos\theta \ln (1 + I_N/\beta I_C)$$

where λ is the photoelectron effective attenuation length, θ is a photo electron emission angle, and $\beta = I_{N,\infty}/I_{C,\infty} \sim 1$ is the ratio of the intensities of the C 1s peak for the nitride peak for an infinity thick nitride carbon sample to that of the substrate peak for a nitrogen-free carbon sample [28]. From the change of C 1s peak component, the values of $\ln (1 + I_N/\beta I_C)$ as a function of $1/\cos\theta$ were plotted in Fig. 3. 14. The $\cos\theta \ln (1 + I_N/\beta I_C)$ was 0.27, which was obtained from inclination of the approximation straight line, and λ of C 1s is ~ 1.8 nm. The doping depth $d \sim 0.49$ nm was roughly calculated from these values, which compared with about two layers of graphene sheets.
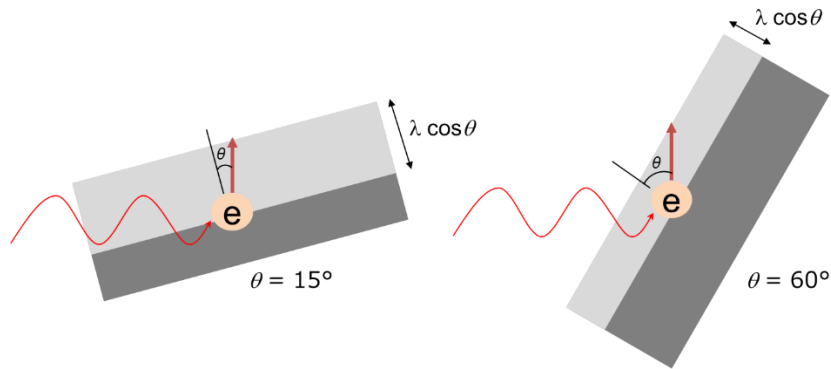
Fig. 3. 12 Schematic illustration of angle-resolved XPS.
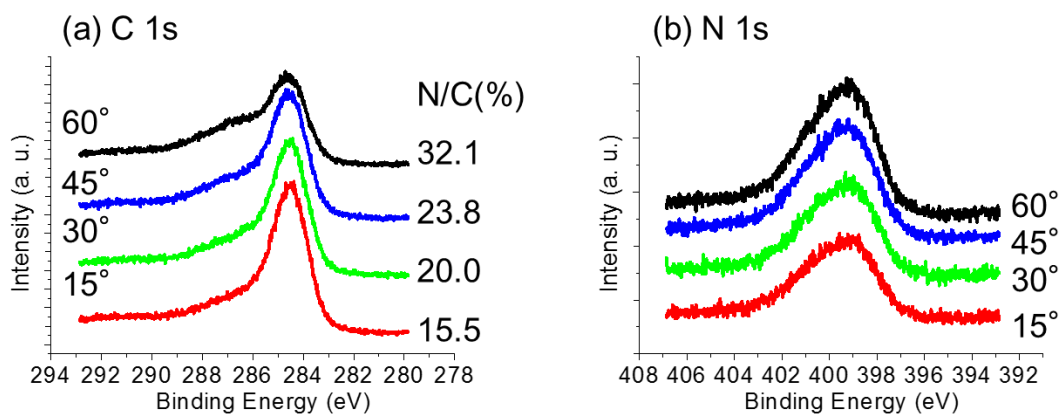
Fig. 3. 13 C 1s (a) and N 1s (b) XPS spectra of N doped HOPG

measured at various emission angles.

Fig. 3. 14 Plots of ln (1 + $I_N/\beta I_C$) as a function of 1/cosθ

derived from C 1s AR-XPS spectra.

3.4   Conclusion

In summary, we examined nitrogen doping to p- and d- HOPG samples to investigate the effect of nitrogen doping amounts and sites on electronic states. Nitrogen doping at a graphitic site is dominant for the defect-free graphene lattice, while doping at a pyridinic site occurs for the defective graphene lattice. The work function has been found to strongly correlate with the nitrogen doping site. Doping at a graphitic site decreases the work function, while doping at a pyridinic or pyrrolic site increases the work function. The present nitrogen plasma treatment could adjust the work function of graphene from 4.3 eV to 5.4 eV. The control of work function would open a way to use the modified graphene for various applications.

Reference

1. Jin, Z., Yao, J., Kittrell, C. & Tour, J. M. Large-scale growth and characterizations of nitrogen-doped monolayer graphene sheets. *ACS Nano* **5,** 4112–4117 (2011).

2. Imamura, G. & Saiki, K. Synthesis of Nitrogen-Doped Graphene on Pt(111) by Chemical Vapor Deposition. *J. Phys. Chem. C* **115,** 10000–10005 (2011).

3. Terasawa, T. & Saiki, K. Synthesis of Nitrogen-Doped Graphene by Plasma-Enhanced Chemical Vapor Deposition. *Jpn. J. Appl. Phys.* **51,** 055101 (2012).

4. Schiros, T. *et al.* Connecting dopant bond type with electronic structure in N-doped graphene. *Nano Lett.* **12,** 4025–31 (2012).

5. Wang, X. *et al.* N-Doping of Graphene Through Electrothermal Reactions with Ammonia. *Science (80).* **324,** 768–771 (2009).

6. Wang, Y., Shao, Y., Matson, D. W., Li, J. & Lin, Y. Nitrogen-doped graphene and its application in electrochemical biosensing. *ACS Nano* **4,** 1790–1798 (2010).

7. Jeong, H. M. *et al.* Nitrogen-doped graphene for high-performance ultracapacitors and the importance of nitrogen-doped sites at basal planes. *Nano Lett.* **11,** 2472–2477 (2011).

8. Lin, Y.-C., Lin, C.-Y. & Chiu, P.-W. Controllable graphene N-doping with ammonia plasma. *Appl. Phys. Lett.* **96,** 133110 (2010).

9. Shao, Y. *et al.* Nitrogen-doped graphene and its electrochemical applications. *J. Mater. Chem.* **20,** 7491 (2010).

10. Favaro, M. *et al.* Palladium nanoparticles supported on nitrogen-doped HOPG: a surface science and electrochemical study. *Phys. Chem. Chem. Phys.* **15,** 2923–31 (2013).

11. Favaro, M. *et al.* Electrochemical behavior of N and Ar implanted highly oriented pyrolytic graphite substrates and activity toward oxygen reduction reaction. *Electrochim. Acta* **88,** 477–487 (2013).

12. Niwa, H. *et al.* X-ray photoemission spectroscopy analysis of N-containing carbon-based cathode catalysts for polymer electrolyte fuel cells. *J. Power Sources* **196,** 1006–1011 (2011).

13. Wang, X. *et al.* Selective nitrogen doping in graphene: Enhanced catalytic activity for the oxygen reduction reaction. *Phys. Rev. B* **84,** 245434 (2011).

14. Fujimoto, Y. & Saito, S. Formation, stabilities, and electronic properties of nitrogen defects in graphene. *Phys. Rev. B - Condens. Matter Mater. Phys.* **84,** 1–7 (2011).

15. Ferrari, A. & Robertson, J. Interpretation of Raman spectra of disordered and amorphous carbon. *Phys. Rev. B* **61,** 14095–14107 (2000).

16. Zhou, Y. *et al.* Dopant-Induced Electronic Structure Modification of HOPG Surfaces: Implications for High Activity Fuel Cell Catalysts. *J. Phys. Chem. C* **114,** 506–515 (2010).

17. Schlaf, R., Parkinson, B. A., Lee, P. A., Nebesny, K. W. & Armstrong, N. R. Absence of final-state screening shifts in photoemission spectroscopy frontier orbital alignment measurements at organic/semiconductor interfaces. *Surf. Sci.* **420,** (1999).

18. Holme, T., Zhou, Y., Pasquarelli, R. & O'Hayre, R. First principles study of doped carbon supports for enhanced platinum catalysts. *Phys. Chem. Chem. Phys.* **12,** 9461–8 (2010).

19. Yu, Y.-J. *et al.* Tuning the graphene work function by electric field effect. *Nano Lett.* **9,** 3430–4 (2009).

20. Kang, B., Lim, S., Lee, W. H., Jo, S. B. & Cho, K. Work-Function-Tuned Reduced Graphene Oxide via Direct Surface Functionalization as Source/Drain Electrodes in Bottom-Contact Organic Transistors. *Adv. Mater.* **25,** 5856–5862 (2013).

21. Kondo, T. *et al.* Atomic-scale characterization of nitrogen-doped graphite: Effects of dopant nitrogen on the local electronic structure of the surrounding carbon atoms. *Phys. Rev. B* **86,** 035436 (2012).

22. Kim, K. *et al.* Annealing Effects after Nitrogen Ion Casting on Monolayer and Multilayer Graphene. *J. Phys. Chem. C* **117,** 2129–2134 (2013).

23. Cress, C. D. *et al.* Nitrogen-Doped Graphene and Twisted Bilayer Graphene via Hyperthermal Ion Implantation with Depth Control. *ACS Nano* **10,** 3714–3722 (2016).

24. Ãhlgren, E. H., Kotakoski, J. & Krasheninnikov, A. V. Atomistic simulations of the implantation of low-energy boron and nitrogen ions into graphene. *Phys. Rev. B - Condens. Matter Mater. Phys.* **83,** 1–7 (2011).

25. Sahu, B. B. *et al.* Effectiveness of plasma diagnostic in ultra high frequency and radio frequency hybrid plasmas for synthesis of silicon nitride film at low temperature. *J. Appl. Phys.* **116,** 1–10 (2014).

26. Luo, Z. *et al.* Pyridinic N doped graphene: synthesis, electronic structure, and electrocatalytic property. *J. Mater. Chem.* **21,** 8038 (2011).

27. Krieg, J., Oelhafen, P. & Guntherodt, H. J. Observation of unfilled electron states in alkali graphite intercalation compounds by secondary electron spectroscopy. *Solid State Commun.* **42,** 831–833 (1982).

28. Lu, Z. H. & Mccaffrey, J. P. SiO 2 film thickness metrology by x-ray photoelectron spectroscopy. *Appl. Phys. A Mater. Sci. Process.* **71,** 2764–2766 (1997).

Chapter 4
Hydrogenation to Graphene

第４章は雑誌等で刊行予定のため非公開
５年以内に出版予定

Chapter 5
Surface Modification and Reduction of Graphene Oxide

第５章は雑誌等で刊行予定のため非公開
５年以内に出版予定

Chapter 6
Application to OFET Device

第 6 章は雑誌等で刊行予定のため非公開
５年以内に出版予定

Chapter 7
Concluding Remarks

In this dissertation, I have synthesized surface modified graphene with plasma process, which results to change the work function of graphene. Then, I fabricated highly effective organic FET with work function tuned GO electrodes.

Nitrogen doping to graphene (Chapter 3).

Defect-free and defective HOPG samples were doped nitrogen atoms by N plasma. Nitrogen atoms are initially doped at a graphitic site (inside the graphene) for the defect-free HOPG, while doping to a pyridinic or a pyrrolic site (edge of the graphene) is dominant for the defective HOPG. The amount of doped nitrogen atoms was up to approximately 10%. The work function of graphene correlates strongly with the site and amount of doped nitrogen, which indicated that nitrogen atoms doped at a graphitic site lower the work function, while nitrogen atoms at a pyridinic or a pyrrolic site raise the work function. Control of the plasma treatment time and the amount of initial defect could change the work function of graphite in a range of 4.3 eV to 5.4 eV.

第４，５，６章は雑誌等で刊行予定のため非公開
５年以内に出版予定

Finally, the method of plasma assisted surface modification in this dissertation provides a valuable work function tuning of graphene and would open a way to tailor the nature of graphene for various industrial applications.

Acknowledgement